High-efficiency multi-spot beam generation with an all-fiber SMF-SCF structure

YONGMIN JUNG, 1,* D NATASHA VUKOVIC, 1 D CHRISTOPHE A. CODEMARD, 2 AND MICHALIS N. ZERVAS^{1,2} D

¹Optoelectronics Research Centre, University of Southampton, Southampton SO17 1BJ, UK

²TRUMPF Laser UK Ltd, 6 Wellington Park, Tollbar Way, Hedge End, Southampton SO30 2QU, UK

*ymj@orc.soton.ac.uk

Abstract: We propose an efficient, fully fiber-based method for generating multi-spot beam patterns using single-mode fiber (SMF) and square-core fiber (SCF) structures. This technique leverages multimode interference in the SCF to produce configurable square lattice beam patterns, such as 2×2 , 3×3 , and 4×4 arrays, by simply adjusting the SCF length. Both simulations and experiments at a wavelength of $1060 \, \mathrm{nm}$ validate the approach, demonstrating high power uniformity, minimal loss, and excellent stability across beam configurations. Initial testing of multi-spot laser drilling on metal surfaces shows that increased beam spot counts can significantly enhance processing efficiency. This SMF-SCF structure offers substantial potential for scalable, compact, and high-precision applications in photonics, laser manufacturing, and biomedical imaging, where rapid processing and parallel operation are critical.

Published by Optica Publishing Group under the terms of the Creative Commons Attribution 4.0 License. Further distribution of this work must maintain attribution to the author(s) and the published article's title, journal citation, and DOI.

1. Introduction

The demand for multiple beam spot generation continues to grow in optical technology, driven by its wide-ranging applications in material processing, optical communications, particle trapping, microscopy, and spectroscopy [1–7]. In laser material processing, simultaneous multi-spot generation enhances operational speed in cutting, drilling, surface treatment, and welding, thereby improving throughput and reducing costs [1–4]. This capability is especially valuable in industrial settings, where efficient processing of multiple areas in parallel reduces operational time, energy consumption, and expenses. In microscopy, particularly in advanced fluorescence microscopy and optical coherent tomography, multi-spot generation facilitates parallel imaging, enabling simultaneous illumination and observation across different regions of a sample [7]. This parallelism is critical for studying dynamic biological processes, where real-time monitoring and capturing transient events over large field of view are essential. Moreover, using multiple beam spots can enhance imaging resolution and improve signal-to-noise ratios by averaging multiple observations.

Conventional multi-spot beam generation methods rely on complex free-space optics, including beam splitters, diffractive optical elements, and spatial light modulators [1–7]. While effective, these methods are often complex, bulky, require precise alignment, and are sensitive to environmental perturbations, making them less practical for large-scale applications. Free-space optics setups are typically costly and lack the compactness necessary for integration into advanced systems. Additionally, beam splitters and spatial light modulators suffer from energy losses and limited efficiency due to inherent design constraints, complicating their use and reducing their flexibility by requiring external components. In recent years, all-fiber systems have emerged as promising alternatives, offering enhanced compactness and integrability. For example, circular multi-spot patterns have been achieved using an adjustable mechanical transducer to convert the fundamental LP₀₁ mode of the fiber to higher-order LP_{n1} modes (n = 3, 4, 5, and 6), constrained

by the numeral aperture (NA) of the cutting head [8,9]. These all-fiber beam shapers have been shown to operate at multi-kilowatt power levels, delivering superior cutting and welding performance compared to traditional beam profiles [8]. However, these approaches require specially designed transducers, which increase the complexity of the device.

In this paper, we introduce a highly efficient method for generating multiple beam spots in non-circular arrangements through multimode interference (MMI) in SMF-SCF structures. Our approach allows precise control over square lattice configurations, such as 2×2 , 3×3 , and 4×4 beam arrays, achieved by simply adjusting the SCF length. This technique offers advantages in scalability, flexibility, and ease of implementation over traditional methods. Preliminary results of this work were presented in previous conference papers [10,11]. Simulations and experimental results at 1060 nm demonstrate the SMF-SCF structure's capability to generate uniform, high-efficiency multi-spot beam patterns. This method opens new opportunities in photonics and laser technology, with promising applications in advanced manufacturing, optical communications, and biomedical imaging, where enhanced processing speed, precision and parallel operation are increasingly essential.

2. Proposed SMF-SCF structure

Our proposed SMF-SCF structure consists of a short segment of SCF spliced to an SMF, as shown in Fig. 1(a). Unlike conventional SMF and multimode fiber (MMF) structure [12,13] that produce circularly symmetric beam patterns, the SMF-SCF structure exploits the multimode properties of the SCF to generate distinct square $N \times N$ lattice beam arrays [14,15]. In this configuration, the SCF acts as a multimode waveguide, allowing selective excitation of multiple transverse modes from the SMF's single-mode input. This leads to the self-imaging of the input beam at well-defined positions along the SCF length. For a general asymmetric input beam, both symmetric and anti-symmetric SCF modes are excited, resulting in $N \times N$ replicas of the input field at distances analytically determined by [16,17]:

$$L_N^{asym} = \frac{4n_{co}W_{eff}^2}{N\lambda_0} \tag{1}$$

where n_{co} is the refractive index of the core, W_{eff} is the effective width of the SCF, λ_0 is the wavelength of the light in a vacuum, and N represents the number of replicated images. In the special case of symmetric input beams, only symmetric SCF modes are excited. As a result, the corresponding self-imaging distances are reduced to a quarter of those for general asymmetric input beams, and the position of $N \times N$ replica is analytically determined by [16,17]:

$$L_N^{sym} = \frac{n_{co}W_{eff}^2}{N\lambda_0} \tag{2}$$

The effective width (W_{eff}) is defined as $W_{eff} = W + 2\delta_{eff}$, where W is the physical width of the SCF core, and δ_{eff} is the effective evanescent field penetration depth into the surrounding cladding. The penetration depth depends on the mode order m (see Appendix) and can be approximated as $\delta_{eff} = (1/M_{exc}) \sum_{m=0}^{M_{exc}} \delta_m$, where M_{exc} is the number of excited modes. For centered, symmetric excitation, the number of excited modes $M_{exc} \propto W/d$, where d is the width of the input waveguide (or core diameter) [18].

At the $N \times N$ lattice plane positions, the coordinates of the (i, j) self-image are approximated by [17]:

$$(x_i, y_j) = \left(\left[-\frac{W_{eff}}{2} + \frac{W_{eff}}{2N} (2i - 1) \right], \left[-\frac{W_{eff}}{2} + \frac{W_{eff}}{2N} (2j - 1) \right] \right), i, j = 1, 2, \dots, N$$
 (3)

The outermost self-images in the N × N replicas are located at a distance $W_{e\!f\!f}/(2N)$ from the SCF core edges, with inter-image distances along each row or column approximated as $W_{e\!f\!f}/N$.

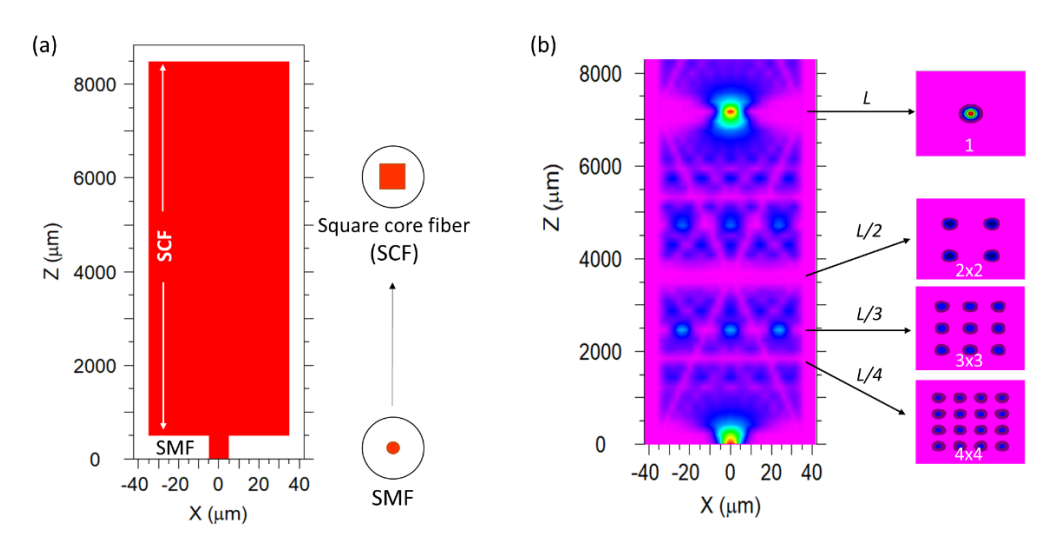


Fig. 1. The proposed SMF-SCF structure for multi-spot beam generation, with (b) simulated beam propagation and intensity profiles at various points along the structure. Waveguide width $W = 70 \, \mu \text{m}$, NA = 0.22, $\lambda_0 = 1064 \, \text{nm}$.

Beam propagation simulations using RSoft were performed to visualize the beam intensity along the SCF. As shown in Fig. 1(b), the symmetric input Gaussian-like beam from the SMF diverges at the SCF-SCF interface and undergoes modal interference within the multimode SCF, producing self-imaging and multi-spot patterns. By carefully adjusting the SCF length, specific beam replication patterns (N × N) can be achieved at various positions along the propagation path: 4-fold (2 × 2) at $L_2^{sym} = L/2$, 9-fold (3 × 3) at $L_3^{sym} = L/3$, and 16-fold (4 × 4) at $L_4^{sym} = L/4$, where $L = L_1^{sym}$ represents the self-imaging length for symmetric mode excitation in the SCF. This ability to control the SCF length allows flexible generation of multi-spot profiles in square lattice formations. With an optimized SCF length, a power redistribution efficiency of 99.8% was achieved, with minor losses attributed to computational approximations or potential coupling to leaky SCF modes. In this study, we used a commercially available SCF with a 70 × 70 µm core, a numerical aperture (NA) of 0.22, and a cladding diameter of 115 µm (CeramOptec). The SMF used had a core diameter of ~10 µm and an NA of 0.085, operated at $\lambda_0 = 1064$ nm. Under these conditions, the analytically calculated self-imaging distance using Eq. (2) is $L_1^{sym} \sim 7052$ µm, which closely matches the numerically calculated values shown in Fig. 1(b).

2.1. Impact of SCF design parameters and device fabrication tolerance

As discussed above, the center-to-center spacing between adjacent beam spots in an $N \times N$ lattice is approximately 1/N of the SCF's core effective width, indicating a direct relationship between core size and spot separation. In this study, we focused on generating a 2×2 beam pattern to examine the influence of the SCF core dimensions on beam separation. As shown in Fig. 2(a), the beam spacing is roughly half the SCF core width (W), with a slight increase due to the Goos-Hänchen effect [12], where light marginally extends into the cladding, resulting in $W_{\rm eff}$ (see Appendix for derivations). All other parameters, such as the SCF's NA and operational wavelength, were held constant for consistency. Increasing the SCF core size widens beam separation but also requires a longer SCF segment to achieve the desired multi-spot pattern. Wavelength dependency was also explored, revealing a modest increase in separation at longer wavelengths, with total variation remaining below 1 μ m. This highlights the structure's wavelength insensitivity across a broad wavelength range from 1 μ m to 1.6 μ m. Additionally, as illustrated in Fig. 2(b), we examined the

impact of the refractive index contrast $(dn = n_{co} - n_{cl})$ within the SCF. While this factor slightly affects beam separation, its influence is minimal compared to that of core size. It is worth noting that the values presented in Fig. 2(a) and (b) are analytically calculated values using Eq. (3) and show excellent agreement with those obtained through the beam propagation method (BPM).

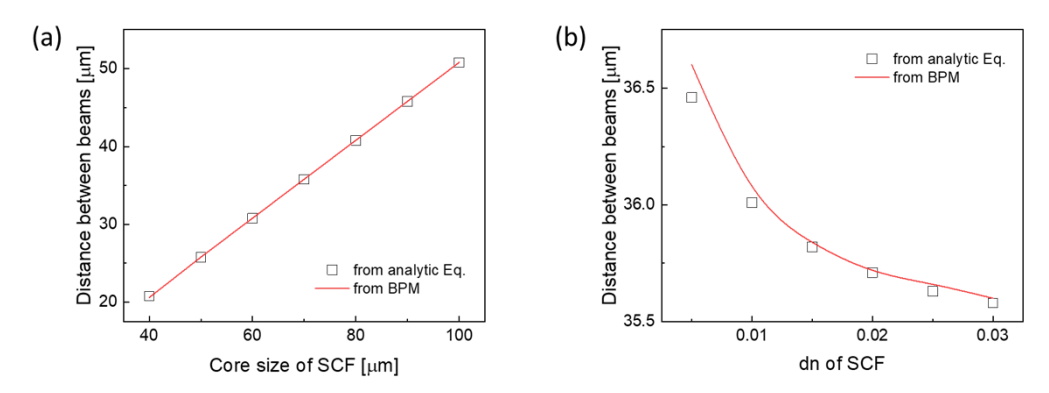


Fig. 2. The impact of (a) core size and (b) refractive index difference between core and cladding of SCF (N = 2).

We further investigated the fabrication tolerance of the SCF length required to produce desired beam patterns (e.g., 2×2). Our simulations indicate that a positional accuracy of approximately $\pm 100~\mu m$ is necessary to achieve over 90% conversion efficiency, as shown in Fig. 3(a). However, in practical applications such as laser material processing, this tolerance is generally less critical. This is because an external optical lens is typically placed at the fiber output to refocus the beam array, allowing users to easily locate and utilize the multi-spot focal plane even if the SCF length is not cleaved with high precision. It is important to note that the multi-spot beam arrays in this structure are generated via MMI-based self-imaging, where each beam spot acts as a near-field replica of the original input field, consistent with the Talbot effect. As a result, the spot size and NA of each replicated beam closely match those of the SMF input. Accurate alignment of the SMF core to the center of the SCF is also crucial, and the quality of the SCF-SCF splice significantly affects performance. Our simulation shows that achieving >90% conversion efficiency requires a core offset of less than 1 μ m and a fiber cleave angle deviation of no more than 0.7 degrees, as shown in Fig. 3(b, c). Maintaining these alignment tolerances are also essential to ensure uniform power distribution across the generated beam spots.

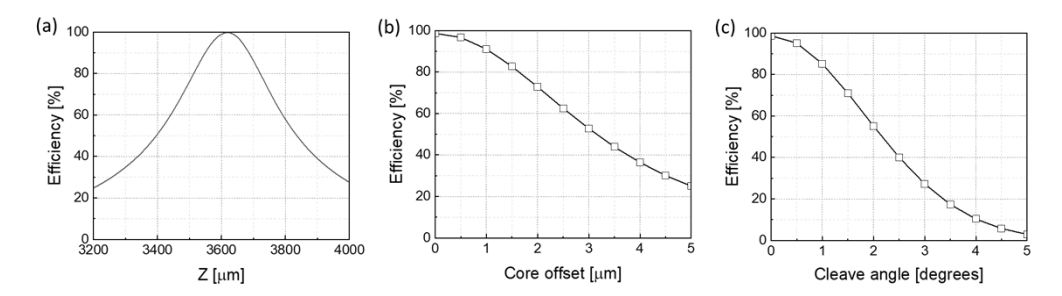


Fig. 3. Device fabrication tolerances of the SMF-SCF structure: (a) sensitivity to SCF length variation, (b) effect of core offset between SMF and SCF, and (c) impact of fiber cleave angle deviation.

2.2. Experimental validation

For experimental validation, we spliced a commercially available SCF with a $70 \times 70 \mu m$ core to an SMF. A microscopic examination of the SCF cross-section, shown in Fig. 4(a), confirmed a central core size of $\sim 70 \times 70 \mu m$, with slightly larger dimensions ($\sim 71.5 \mu m$) observed at the edges. Although the SCF corners were slightly rounded, this had a negligible impact on our application. Precise SCF lengths were obtained using an advanced cleaver with a micropositioner, providing position accuracy around 10 µm, which was essential for achieving the targeted lengths and consistent multi-spot patterns. After fabrication, near-field beam patterns at 1060 nm were recorded using a super-luminescent diode and a CCD camera. Figure 4(b) displays experimental results showing uniform, symmetric distributions of 2×2 , 3×3 , and 4×4 beam spots, validating the SMF-SCF structure's effectiveness in generating multi-spot arrays. To quantitatively assess power distribution, CCD-captured images were analyzed, measuring photon counts from individual pixels during camera exposure to evaluate power variations. The analysis revealed an almost uniform power distribution across all beams, with variations under 0.9 dB, highlighting the stability and efficiency of the SMF-SCF structure in producing well-balanced multi-spot patterns. Additionally, the SCF lengths used to experimentally achieve the $N \times N$ lattice patterns showed excellent agreement with the valued obtained through both analytical calculations and numerical simulations.

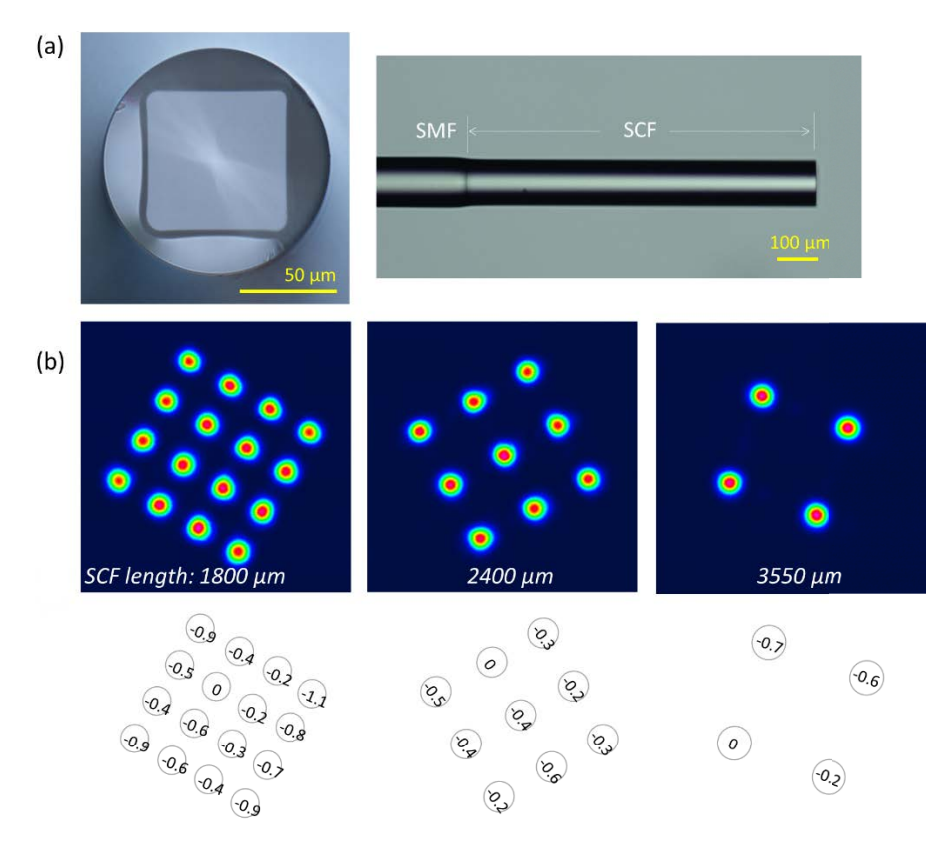


Fig. 4. (a) Cross-section of the SCF and SMF-SCF structure. (b) Measured beam profiles and corresponding power distributions (in dB scale) for SMF-SCF samples with 2×2 , 3×3 , and 4×4 spot arrays.

2.3. Material processing applications

To evaluate the potential of the multi-spot beam generated by the SMF-SCF structure for material processing, we employed a 1064 nm pulsed laser system consisting of a fiber-pigtailed microchip laser and a single stage fiber amplifier. This setup delivered 1.2 ns pulses at a 100 kHz repetition rate, with a peak power of \sim 5 kW. The output fiber, featuring a single-mode 10 μ m core, was directly spliced to the SMF-SCF structure, ensuring seamless beam delivery. The multi-spot output beam was directed through the entrance lens of an Ophir BeamSquared beam profiler to visualize the spatial evolution of the beam intensity profile in a plane perpendicular to the propagation axis. As shown in Fig. 5(a), the 2×2 beam pattern is clearly observed near the focal region, maintaining its spatial distribution within the Rayleigh range. Beyond this region, the pattern evolves into a 3×3 configuration, consistent with the expected far-field image of the 2 × 2 beam. Although the Ophir BeamSquared system is primarily designed for near-Gaussian beam profiles and applies the second-moment method to calculate beam quality, it was employed here to qualitatively monitor the beam propagation behavior. Beam quality factors (M²) were measured for the 2×2 , 3×3 , and 4×4 patterns, yielding approximate values of 6.6, 8, and 7, respectively. While these M² values do not represent absolute beam quality due to the multi-spot nature of the beams, they provide useful comparative insights into the spatial characteristics and propagation dynamics of the SMF-SCF generated patterns.

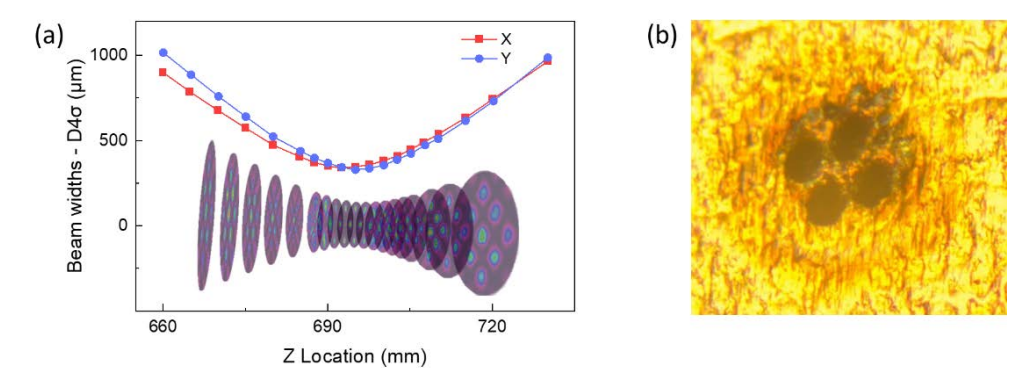


Fig. 5. (a) Visualization of beam evolution based on M^2 measurement for the 2×2 SMF-SCF structure. (b) Drilled holes of $10 \, \mu m$ -thick copper foils at the focal point.

To assess the structure's practical utility for material processing, we conducted preliminary laser drilling tests on copper foils. By optimizing the focal distance, we maintained the desired beam pattern to maximize material interaction. As shown in Fig. 5(b), the 2×2 beam array created four cleanly drilled holes, each with a diameter of $\sim 4~\mu m$, in a 10 μm -thick copper foil. Successful hole formation was verified by illuminating the sample with a collimated green laser and observing diffraction patterns consistent with theoretical expectations. This verification confirmed both the quality and uniformity of the ablation. Ongoing research aims to expand this multi-spot approach to a broad range of materials and further refine processing parameters. The SMF-SCF structure shows significant promise for advanced material processing applications, including micro-machining, surface treatment, and controlled ablation, where multi-spot beam configurations can improve throughout and precision.

2.4. Design flexibility of the proposed structure

The proposed SMF-SCF structure demonstrates remarkable scalability and adaptability, supporting a diverse range of multi-beam configurations. For instance, employing an SCF with a large core, such as $150 \times 150 \,\mu m$ core, enables the generation of extensive multi-beam arrays, allowing

configurations with over a 10×10 beam array, as shown in Fig. 6(a). Additionally, by modifying the SCF core geometry to non-square shapes, such as rectangular or hexagonal, the structure can produce multi-beam lattice patterns that align with the aspect ratios of these arrangements. This feature greatly enhances the design's versatility for applications that demand specific beam patterns. A key advantage of this design is its ability to form linear (one-dimensional) beam arrays by precising adjusting the dimensions of a rectangular-core fiber. For example, a rectangular core of 50×10 µm can produce a linear array of beam spots, as demonstrated by the four-spot array shown in Fig. 6(b). This configuration is ideal for applications requiring line-focused energy distribution, broadening the utility of the structure in material processing and imaging applications. The design's flexibility extends further with the option to replace the single-mode input fiber with a few-mode fiber, enabling the generation of multiple high-order mode beams. As shown in Fig. 6(c), launching high-order modes (e.g. LP₂₁ modes) through a few-mode fiber input allows for creation of an array of LP21 beams at the SCF output. This adaptability offers significant advantages in applications requiring tailored intensity distributions or advanced beam shaping, highlighting the versatility of the SMF-SCF structure for complex, customized multi-beam configurations. Furthermore, the regular multi-spot beams generated by this approach could be applied to particle trapping applications, such as neutral atom tweezer arrays and ion arrays, where precise and efficient beam splitting is essential. Additionally, space division multiplexing and coherent beam combination systems may benefit from the ability to efficiently split and combine beams using SCFs. Related studies on beam combination and SMF-to-multicore fiber splitting using SCFs have been reported [19,20]. Our work extends this concept by demonstrating a scalable method for generating large arrays of beam spots, along with a direct demonstration of its applicability to laser material processing.

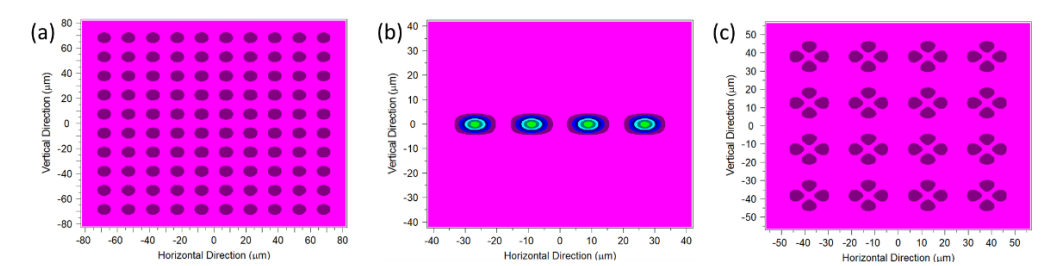


Fig. 6. Examples showcasing design flexibility: (a) generation of a large number of multi-beams, (b) one-dimensional multi-beam arrangement, and (c) multiple beams with higher-order modes.

3. Conclusion

We have demonstrated a versatile and efficient SMF-SCF structure capable of generating precise multi-spot beam patterns. By adjusting SCF length and core geometry, this structure enables diverse lattice beam configurations, including square and non-square arrays, with high uniformity and minimal power loss. Experimental validation at 1060 nm confirmed the stability and effectiveness of the multi-spot patterns, while preliminary material processing tests highlighted the potential for high-precision applications, such as copper foil drilling. The SMF-SCF structure's compact design, scalability, and adaptability represent a significant advancement in beam shaping technology. Its ability to produce complex, customized beam arrays without the need for bulky free-space optics makes it particularly suitable for applications across photonics, laser technology, and advanced manufacturing. With promising applications in areas where speed, precision, and parallel processing are critical, the SMF-SCF structure opens new avenues for innovation in optical systems design and advanced material processing.

Appendix: Evanescent field penetration depth & effective waveguide thickness

The presence of an evanescent field in guided waveguide modes is well-established and is associated with an effective penetration depth into the cladding, which contributes to an increase in the effective waveguide thickness [21]. Figure 7 illustrates a schematic of a symmetric multimode waveguide with a core thickness of W, core refractive index n_{co} , and cladding refractive index n_{cl} . The waveguide is symmetrically excited by a single-mode waveguide with a width d.

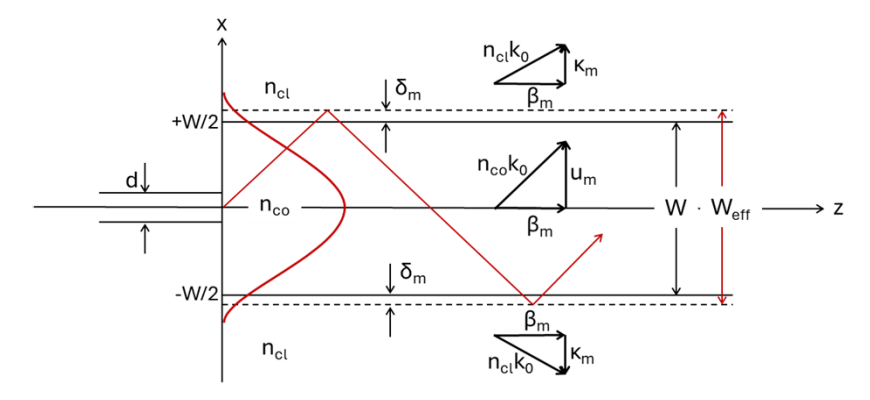


Fig. 7. Schematic of a symmetric multimode slab waveguide with a thickness W, core (cladding) refractive index n_{co} (n_{cl}), symmetrically excited by a single-mode waveguide with a width d.

The electric field of the m^{th} guided TE mode is described as [19]:

$$E_{mx} = \begin{cases} A_m \cos(u_m W/2 - \phi_m) \exp[-\kappa_m (x - W/2)]; & (x > + W/2) \\ A_m \cos(u_m x - \phi_m); & (-W/2 \le x \le + W/2) \\ A_m \cos(u_m W/2 + \phi_m) \exp[+\kappa_m (x + W/2)]; & (x < - W/2) \end{cases}$$
(4)

where

$$u_{m} = \sqrt{n_{co}^{2}k_{0}^{2} - \beta_{m}^{2}}$$

$$\kappa_{m} = \sqrt{\beta_{m}^{2} - n_{cl}^{2}k_{0}^{2}}$$
(5)

are the transverse wavenumbers, with n_{co} and n_{cl} being the core and cladding refractive indices, respectively. Here, $\beta_{\rm m}$ represents the mode propagation constant, and $k_0 = 2\pi/\lambda_0$. By applying boundary conditions at $x=\pm W/2$, the dispersion relation is obtained:

$$U_m = \frac{m\pi}{2} + \tan^{-1}\left(\frac{K_m}{U_m}\right)$$

$$\phi_m = \frac{m\pi}{2}$$
(6)

where $U_m = u_m W/2$ and $K_m = \kappa_m W/2$, and $m = 0, 1, 2, ..., M_{\text{max}}$. For well-guided modes, where $K_m \gg U_m$ and $\tan^{-1}(K_m/U_m) \approx \pi/2$, the dispersion relation simplifies to:

$$U_m \approx \frac{(m+1)\pi}{2} \tag{7}$$

The evanescent field penetration depth into the cladding is defined as $\delta_m = 1/\kappa_m$. By substituting Eq. (7) into Eq. (5), the penetration depth becomes:

$$\delta_m = \frac{1}{k_0 \sqrt{(n_{co}^2 - n_{cl}^2) - \frac{(m+1)^2 \lambda_0^2}{4W^2}}}, (m = 0, 1, 2, \dots, M_{\text{max}})$$
(8)

where M_{max} is the number of guided modes. The cladding penetration depth can also be expressed as:

$$\delta_m = \frac{W}{2\sqrt{V^2 - \frac{(m+1)^2 \pi^2}{4}}}, \quad (m = 0, 1, 2, \dots, M_{\text{max}})$$
 (9)

where $V = k_0(W/2)\sqrt{n_{co}^2 - n_{cl}^2} = k_0(W/2)NA$ is the normalized frequency. Figure 8 illustrates the cladding penetration depth for waveguides with NA = 0.22 and λ_0 = 1064 nm for various core widths. Across all core widths, the penetration depth is slowly varying with the mode order when $m << M_{\text{max}}$ (well-guided modes) but increases sharply as $m \to M_{\text{max}}$, where the modes approach the cut-off condition.

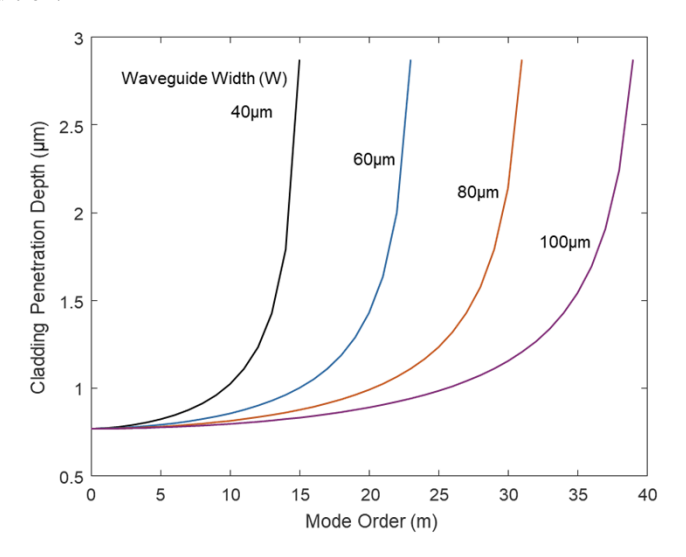


Fig. 8. Cladding penetration depth for waveguides with NA = 0.22, λ_0 = 1064 nm, and different waveguide widths.

The average penetration depth across all guided modes is approximately 2.1 μ m, irrespective of the waveguide width. However, when averaged over the excited modes (M_{exc}), the penetration depth is reduced to approximately 0.78 μ m, also independent of the waveguide width. For centered, symmetric excitation, $M_{exc} \propto W/d$, where d is the width of the input waveguide (or core diameter) [18].

Funding. Engineering and Physical Sciences Research Council (EP/W028786/1).

Disclosures. The authors declare no conflicts of interest.

Data availability. Data underlying the results presented in this paper are available in [22].

References

- J. Finger and M. Hesker, "High power ultrashort pulse laser processing using a flexible multibeam approach," J. Phys. Photonics 3(2), 021004 (2021).
- 2. F. O. Olsen, K. S. Hansen, and J. S. Nielsen, "Multibeam fiber laser cutting," J. Laser Appl. 21(3), 133-138 (2009).

- 3. N. Grubert, F. Lange, J. Stollenwerk, *et al.*, "Enhancing laser materials processing efficiency: dynamic beam shaping and parallelization strategies," *Proc. SPIE* 13005, 1300506 (2024).
- A. Laskin, J. Volpp, V. Laskin, et al., "Beam shaping of high power multimode lasers by multi-spot optics," Proc. SPIE 13005, 1300507 (2024).
- P. Polynkin, A. Peleg, L. Klein, et al., "Optimized multiemitter beams for free-space optical communications through turbulent atmosphere," Opt. Lett. 32(8), 885–887 (2007).
- H. Misawa, K. Sasaki, M. Koshioka, et al., "Multibeam laser manipulation and fixation of microparticles," Appl. Phys. Lett. 60(3), 310–312 (1992).
- C. Zhou, A. Alex, J. Rasakanthan, et al., "Space-division multiplexing optical coherence tomography," Opt. Express 21(16), 19219–19227 (2013).
- 8. N. Vukovic, J. S. Chan, C. A. Codemard, *et al.*, "Multi-kW fiber laser with azimuthal mode output beam for advanced material processing," *Proc. SPIE* 11266, 1126618 (2020).
- N. Vukovic, J. S. Chan, C. A. Codemard, et al., "Fibre-delivered kilowatt petal beams with self-healing properties," Proc. SPIE 11672, 116720U (2021).
- Y. Jung, N. Vukovic, C. A. Codemard, et al., "Multispot fiber lasers for material processing applications," Proc. SPIE 12865, 128650B (2024).
- Y. Jung, N. Vukovic, C. A. Codemard, et al., "Efficient multibeam generation in square lattices using SMF-SCF structure." Proc. SPIE 12871, 128710D (2024).
- L. B. Soldano and E. C. M. Pennings, "Optical multi-mode interference devices based on self-imaging: principles and applications," J. Lightwave Technol. 13(4), 615–627 (1995).
- Y. O. Yilmaz, A. Mehta, W. S. Mohammed, et al., "Fiber-optic beam shaper based on multimode interference," Opt. Lett. 32(21), 3170–3172 (2007).
- Z. Zhang, J. Fiebrandt, D. Haynes, et al., "Fiber-based three-dimensional multi-mode interference device as efficient power divider and vector curvature sensor," J. Opt. 20(3), 035701 (2018).
- 15. K. Wang, X. Dong, P. Kienle, *et al.*, "Optical fiber sensor for temperature and strain measurement based on multimode interference and square-core fiber," Micromachines **12**(10), 1239 (2021).
- R. Ulrich and G. Ankele, "Self-imaging in homogeneous planar optical waveguides," Appl. Phys. Lett. 27(6), 337–339 (1975).
- R. M. Jenkins, R. W. J. Devereus, and J. M. Heaton, "Waveguide beam splitters and recombiners based on multimode propagation phenomena," Opt. Lett. 17(14), 991–993 (1992).
- R. M. Jenkins, R. W. J. Devereus, and J. M. Heaton, "A novel waveguide Mach-Zehnder interferometer based on multimode interference phenomena," Opt. Commun. 110(3-4), 410–424 (1994).
- S. Liang, J. D. Downie, S. Makovejs, et al., "Efficient SMF-to-MCF power splitter using multimode interference in square core fiber," OFC'25, W4J.2 (2025).
- 20. Y. Yan, Y. Liu, H. Zhang, *et al.*, "Principle and numerical demonstration of high power all-fiber coherent beam combination based on self-imaging effect in a square core fiber," Photonics Res. **10**(2), 444–455 (2022).
- 21. K. Okamoto, Fundamentals of Optical Waveguides (Elsevier Inc., 2006).
- Y. Jung, "High-efficiency multi-spot beam generation with an all-fiber SMF-SCF structure: data," University of Southampton, 2025, https://doi.org/10.5258/SOTON/D3467.